Urban Climate 53 (2024) 101834

Contents lists available at ScienceDirect

Urban Climate

journal homepage: www.elsevier.com/locate/uclim

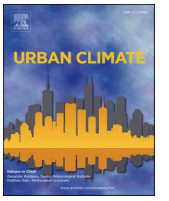

The London pollution island under Lamb weather types

Isidro A. Pérez *, Mª. Ángeles García, Saeed Rasekhi, Fatemeh Pazoki

Department of Applied Physics, Faculty of Sciences, University of Valladolid, Paseo de Belén, 7, 47011 Valladolid, Spain

ARTICLE INFO

Keywords:
Urban pollution island
Kernel smoothing
Background concentrations
Synoptic types

ABSTRACT

This study considers the daily values of gridded concentrations for NO_2, O_3, PM_{10} and $PM_{2.5}$ in London and its surroundings over 2007–2011. A two-step procedure was used for concentration smoothing to observe the urban pollution island. In the first step, the elliptic fit was compared with fits from the Gaussian and Epanechnikov kernels. The results obtained for the Gaussian kernel were used to apply an elliptic fit and a Gaussian directional fit. Lamb weather types were also determined. As a result, the elliptic fit calculated extended concentrations against those calculated with the kernels, and the Gaussian kernel provided a smoother shape. NO_2 and O_3 presented the opposite distribution, and the urban pollution island was defined with contrasted concentration values between the city centre and the surrounding areas. The second smoothing simplified the urban shape and determined the background concentrations. The most frequent type was the anticyclonic, although the most contrasting result was obtained for the anticyclonic type with SE flow, since O_3 values were low compared to the high NO_2 values, thereby revealing pollution transport from the continent under this infrequent type. Finally, the urban pollution island shape is maintained for NO_2 and O_3 under the most frequent weather types.

1. Introduction

Cities are hotspots of air pollution. However, the concentrations measured at these sites are not only the result of urban sources of pollutants, since pollution transport from other sources may also make a noticeable contribution. Moreover, some meteorological variables may affect the values measured.

Urban-rural contrast may be calculated following a procedure similar to that presented by Han et al. (2023), in which pairs of urban and nonurban sites were formed where each urban site was paired with a suburban site in a 50 km radius, and with a rural site at a distance of 100 km. With this method, the authors found that urban-nonurban ozone differences had decreased over the last 30 years. Ivanovski et al. (2023) classified stations in Slovenia following the origin of pollution stemming from traffic, industrial and background sources. The authors obtained the greatest NO_2 and PM_{10} concentrations for the traffic station, whereas the values of the industrial station lay between those of two background stations. Another question to be considered is city size, since the urban-rural contrast is usually evaluated for major cities. However, small towns should not be ignored, since they may be transport nodes or even tourism centres, such that pollution levels can occasionally be high (Tammekivi, Kaasik, Hamer, Santos, and Šteinberga, 2023).

The temperature contrast between the city and its surrounding area determines the urban heat island. Recent studies indicate that some cities are cool islands during the day, whereas the urban heat island is formed during the night. Ashraf, El Seoud, Sodoudi, and El Zafarany (2023) reported this effect for Cairo, Egypt, which is surrounded by desert to the east and west, and farmland to the north and

* Corresponding author.
E-mail address: isidro.perez@uva.es (I.A. Pérez).

https://doi.org/10.1016/j.uclim.2024.101834
Received 4 July 2023; Received in revised form 31 October 2023; Accepted 4 February 2024
Available online 9 February 2024

south. During the daytime, the city temperature is between the desert and farmland temperatures. Similar behaviour was also observed during summer daytime at Bhopal, India, whereas, the opposite –i.e. the urban heat island– was observed at Guwahati, India (Mohammad and Goswami, 2023). Both responses may be explained by the influence of evapotranspiration on the urban heat island and the croplands surrounding the cities. Droste, Steeneveld, and Holtslag (2018) introduced the urban wind island, and Milelli et al. (2023) presented the urban dry island for Turin, Italy. Since the contrast between cities and their surrounding areas may be extended to other meteorological variables such as the boundary layer height, cloud cover or precipitation, Karlický et al. (2020) considered the urban meteorology island. Ulpiani (2021) highlighted the need to explore the synergism between both the heat and the pollution islands, since both are responses of the urban metabolism to thermo-chemical changes triggered by buildings rather than by natural elements.

One initial objective of this research is to delimit the urban pollution island, which is possible using satellite images. Bakaeva and Le (2022) followed this procedure to investigate $PM_{2.5}$ concentrations at Moscow, Russia. However, this procedure may be complemented by including a low-cost sensor network. Liang et al. (2023) used such a method and considered three types of environment (urban, suburban, and rural) as well as two concentration levels in each environment. The current research uses a dense network modelled from observations for England and Wales (Mukhopadhyay and Sahu, 2018). As a result of the urban pollution island, the background concentrations surrounding a city may be established.

Different studies point to the close relationship between meteorology and pollutant concentrations. Some of these studies adopt a local focus and scope, such as the analysis of Birim, Turhan, Atalay, and Gokcen (2023), who examined the influence of various meteorological variables on PM_{10} concentrations at two Turkish sites –one urban and the other rural. They found relative humidity to be the most influencing variable at both sites. However, certain studies adopt a regional scope. Qin et al. (2023) reported the transboundary transport of atmospheric particulate bound mercury by the East Asian monsoon over the Beijing-Tianjin-Hebei region, China, where the contribution of west and northwest air masses from central Asia and Russia is noticeable. This kind of pollution is even transported to the ocean, whereas southeast air masses from the ocean in summer dilute this pollution.

The current research explores the impact of weather types on the urban pollution island. Various procedures are available to determine weather types. Some are geared towards specific applications, such as the classification suggested by Cao et al. (2021), which is based on circulation at two levels, 1000 hPa and 700 hPa, and which was developed to study the prescribed burns along the U. S. Gulf of Mexico coast. However, the analysis of Salinger et al. (2022) relates weather types to maize crop yield in Veneto, Italy. This paper considers Lamb weather types, which were proposed for the British Isles (Lamb, 1972). The main feature of this classification is that types may be objectively determined using the procedure proposed by Jenkinson and Collison (1977) once the pressure fields are known. This method has been used in various regions, such as central Europe (Otero, Sillmann, and Butler, 2018), Serbia (Putniković and Tošić, 2018), eastern Siberia, Russia (Osipova and Osipov, 2022), central China (Yan et al., 2021), or southern Chile (Sarricolea, Meseguer-Ruiz, Martín-Vide, and Outeiro, 2018). However, some limitations have been reported, such as its application in areas within 23.5° and 80° latitude (Fernández-Granja, Brands, Bedia, Casanueva, and Fernández, 2023).

Synoptic types are related to a regional scale, although their impact has been analysed at smaller scales. Chen et al. (2022) studied the influence of weather types on ozone concentrations at the Pearl River Delta, China. The current research considers an even smaller

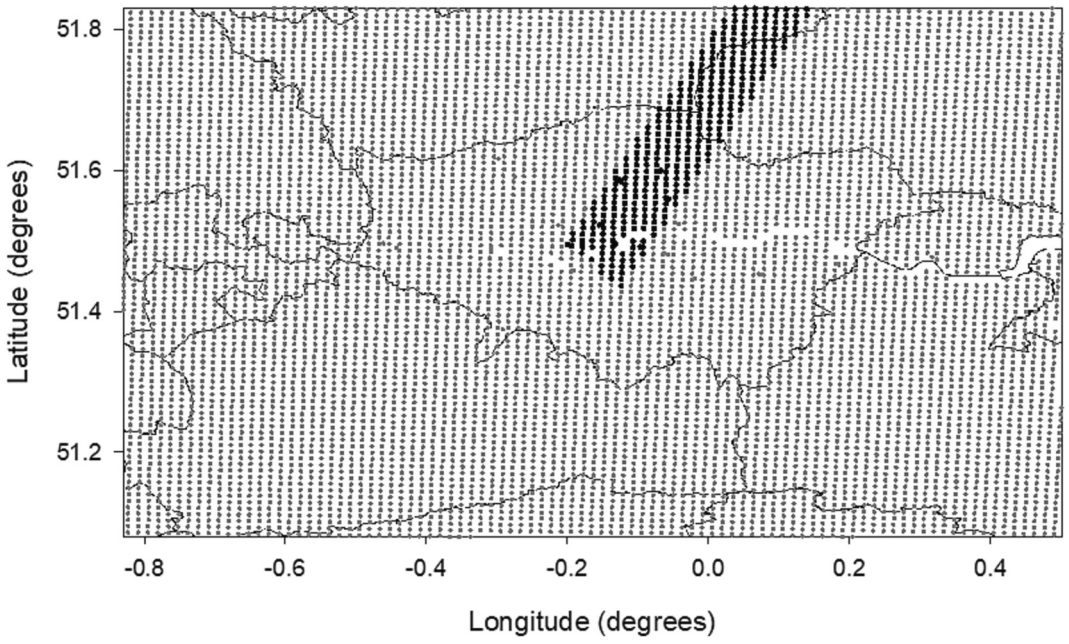

Fig. 1. Network of sites where concentration values are available. Black dots correspond to a 0.1-degree width strip centred in the 35° direction –by way of an example.

scale. The influence of the synoptic pattern on the urban microclimate has already been analysed (Yin et al., 2023). However, this influence on the urban pollution island remains unexplored.

In this paper, the materials and methods section describes not only the region analysed, the pressure fields and the concentration grids, but also the calculation procedures employed to establish the London urban pollution island and how Lamb weather types were determined. Pollution boundaries and background concentrations are established together with the response of different pollutants to the calculation procedure in the results section. Moreover, synoptic patterns in the period analysed are obtained, and the concentrations and urban shapes linked to these patterns are presented in order to improve current knowledge concerning the behaviour of the urban pollution island.

2. Materials and methods

2.1. The concentration database

Daily concentrations of NO_2, O_3, PM_{10} and $PM_{2.5}$ with a spatial resolution of 1 km over the period 2007–2011 were downloaded from the Medical and Environmental Data Mash-up Infrastructure (2023). Although volatile organic compounds (VOC) are essential for studying O_3 pollution, they were not included in the database. The selected region focuses on London, Fig. 1, and extends from 50° 5′ N to 51° 50′ N, and from 0° 50′ W to 0° 30′ E with 7681 grid points.

2.2. Determining the urban pollution island

Three procedures were used. The first fits the concentrations to an exponential function.

$$c(x,y) = a\,exp\left(bx^2 + cy^2 + dxy\right) \tag{1}$$

where c is the concentration at (x,y), which are the spatial coordinates. The intersection of this function at a constant concentration determines the ellipses.

The other procedures use smoothing functions, such as

$$c(x,y,h_1,h_2) = \frac{\sum_{i=1}^{N} K_1\left(\frac{x-x_i}{h_1}\right) K_2\left(\frac{y-y_i}{h_2}\right) c_i}{\sum_{i=1}^{N} K_1\left(\frac{x-x_i}{h_1}\right) K_2\left(\frac{y-y_i}{h_2}\right)} \tag{2}$$

where c is the concentration calculated at point (x,y), c_i is the known concentration at point (x_i,y_i), K_i are the smoothing kernels, and h_i are the windows or bandwidths. Two kernels were used. The first is the Gaussian kernel

$$K(t) = (2\pi)^{-1/2} exp\left(-0.5t^2\right) - 3 < t < 3 \tag{3}$$

Since the Gaussian function extends for all the x-values, the interval calculation was limited to increase the calculation speed (Fernández-Duque, Pérez, García, Pardo, and Sánchez, 2019). The bandwidth –h– was calculated following Silverman's method (Donnelly, Misstear, and Broderick, 2011).

$$h = 0.9\sigma n^{-1/5} \tag{4}$$

where σ is the standard deviation of n data.

The second smoothing equation used the Epanechnikov kernel

$$K(t) = 0.75\left(1 - t^2\right) - 1 \le t \le 1. \tag{5}$$

2.3. Second smoothing

Once smoothing with the Gaussian kernel has been performed, a second smoothing is used to better define the pollution island and to calculate background concentrations. Two procedures were followed. The first considers eq. (1) in order to obtain pollution ellipses surrounded by a nearly uniform background. Varied backgrounds were tried and the one selected corresponded to the highest correlation coefficient between the initial values and those modelled. However, the second procedure is based on directional fitting. The region is divided into strips, such as the one shown in Fig. 1. A total of 360 strips of 0.1-degree width in directions separated by one degree were used. Inside each strip, each point is defined by its direction and distance to the centre. This centre is calculated by a weighted average of all the values for the whole region. Once the concentration centre has been determined, the previous procedure was also followed, i.e., a Gaussian fit was tried, although in this case between the concentration and the radial distance. In addition, a variable background was also considered for each direction. The selection procedure was the same as applied in the first procedure.

2.4. Weather types

Pressure fields at sea level were obtained from the NCEP-NCAR Reanalysis 1 data provided by the NOAA PSL, Boulder, Colorado, USA, through its web page https://psl.noaa.gov. Since the spatial resolution is 2.5°, the region analysed is centred at longitude 0° and latitude 50° N, which is a site close to London, Fig. 2.

The Lamb classification is made up of 27 weather types (Lamb, 1972). However, application of this classification following an objective procedure was presented by Jenkinson and Collison (1977) based on the following expressions:

$$\text{Westerly flow}: W = \frac{1}{2}(P12 + P13) - \frac{1}{2}(P4 + P5) \tag{6}$$

$$\text{Southerly flow}: S = C1\left[\frac{1}{4}(P5 + 2 \times P9 + P13) - \frac{1}{4}(P4 + 2 \times P8 + P12)\right] \tag{7}$$

$$\text{The resulting flow}: F = \left(S^2 + W^2\right)^{1/2} \tag{8}$$

Westerly shear vorticity:

$$ZW = C2\left[\frac{1}{2}(P15 + P16) - \frac{1}{2}(P8 + P9)\right] - C3\left[\frac{1}{2}(P8 + P9) - \frac{1}{2}(P1 + P2)\right] \tag{9}$$

Southerly shear vorticity:

$$ZS = C4\left[\frac{1}{4}(P6 + 2 \times P10 + P14) - \frac{1}{4}(P5 + 2 \times P9 + P13) - \frac{1}{4}(P4 + 2 \times P8 + P12) + \frac{1}{4}(P3 + 2 \times P7 + P11)\right] \tag{10}$$

$$\text{Total shear vorticity}: Z = ZW + ZS \tag{11}$$

where:

$$C1 = 1/cos(latitude) \tag{12}$$

$$C2 = \frac{sin(latitude)}{sin(latitude - 5°)} \tag{13}$$

$$C3 = \frac{sin(latitude)}{sin(latitude + 5°)} \tag{14}$$

$$C4 = \frac{1}{2cos^2(latitude)} \tag{15}$$

Latitude is 50°N in the current application.

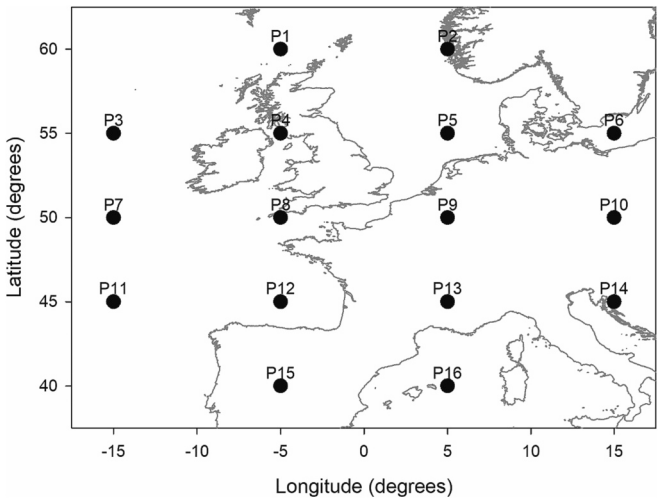

Fig. 2. Network used to determine Lamb weather types.

$$Wind\ direction = tan^{-1}\left(\frac{W}{S}\right)\begin{cases} If\ W > 0\ and\ S < 0, add\ 360^{\circ} \\ If\ S > 0, add\ 180^{\circ} \end{cases} \quad (16)$$

Wind direction is determined in 45° sectors.

If $|Z| < F$, a Lamb pure directional type appears, i.e., northerly, N, north-easterly, NE, easterly, E, south-easterly, SE, southerly, S, south-westerly, SW, westerly, W, and north-westerly, NW.

If $|Z| > 2F$, the weather type is cyclonic, C, ($Z > 0$) or anticyclonic, A, ($Z < 0$).

If $F < |Z| < 2F$, the synoptic situation is a Lamb hybrid type.

If $F < 6$ and $|Z| < 6$, the pattern is the unclassified type, U.

3. Results

3.1. An initial approach to the urban pollution island

Fig. 3 presents the contour plot of the four pollutants; NO_2, O_3, PM_{10}, and $PM_{2.5}$. The contrast between the city centre and its surroundings is quite pronounced for NO_2 and O_3. However, whereas the highest NO_2 values are found in the city centre, the opposite distribution is found for O_3. The most relevant feature of the spatial distribution of particulate matter is the fairly uniform concentrations observed. However, PM_{10} concentrations are slightly higher in the city centre, whereas they are slightly lower for $PM_{2.5}$. The elliptical fit determined noticeable concentrations over areas greater than those obtained with the smoothing kernels. Moreover, the elliptical shape could not be applied with $PM_{2.5}$, perhaps due to the low contrast of concentrations in the region and their complex distribution. The elliptical distribution is quite oriented for NO_2 and O_3, with the main axis along the longitude axis. However, for PM_{10}, the elliptical shape is less extended, with lower eccentricity, and with a higher slope. Table 1 presents the correlation coefficient of these fits, where the lowest values were obtained by the elliptical fit. Moreover, the average concentration at the region corners was used as background concentration and two limits were established by dividing the concentration range into three equal parts. The means for each part are presented in Table 1. The contrast between the highest and the lowest values is around 15, 12, 0.4, and 0.7 μg

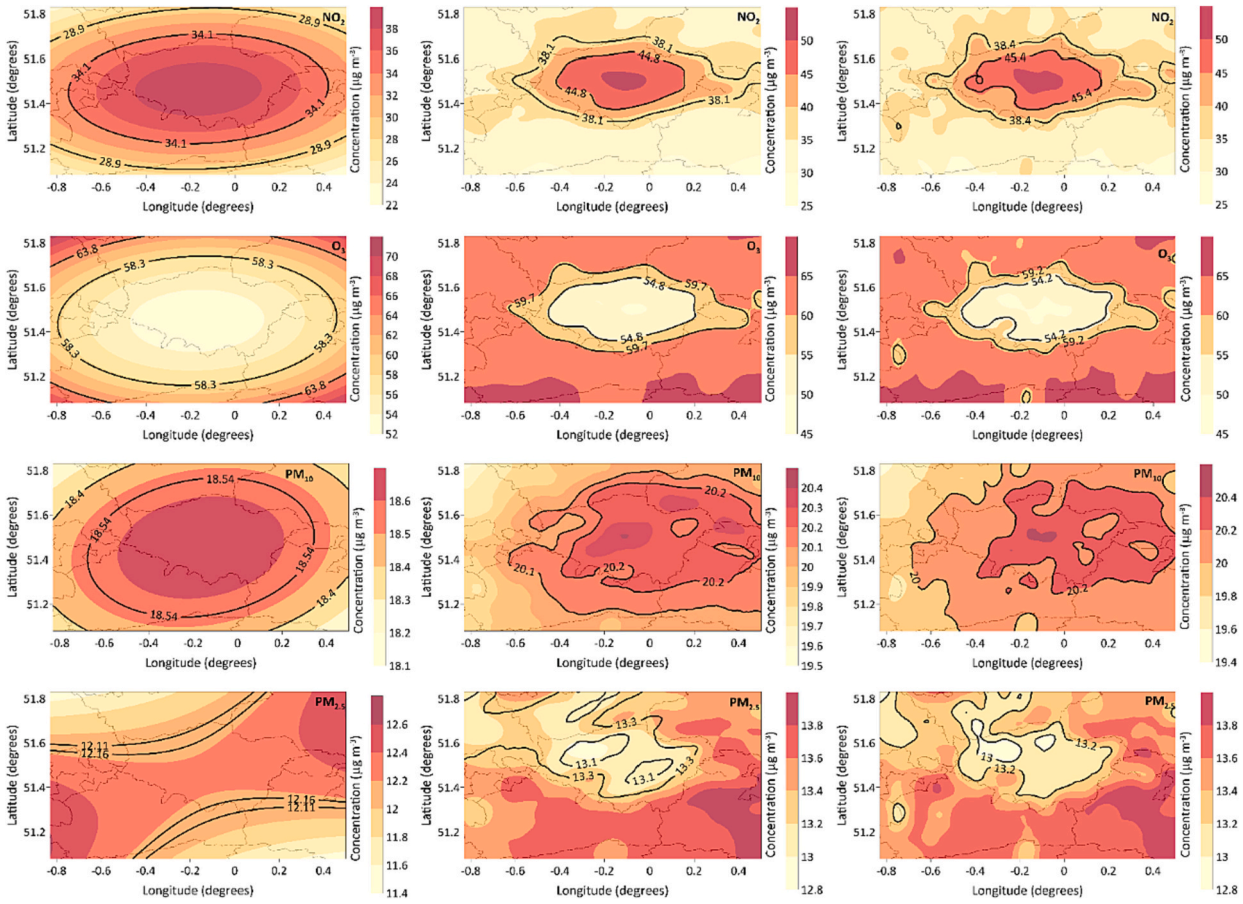

Fig. 3. Fits of the pollutants analysed with the three procedures, elliptical fitting (left column), and smoothings with Gaussian (middle column) and Epanechnikov (right column) kernels. The black contours correspond to one and two thirds of the concentration interval calculated in the region.

Table 1
Mean concentration for the three regions considered in this study, following different fitting procedures.*

	NO_2 (μg m^{-3})				O_3 (μg m^{-3})				PM_{10} (μg m^{-3})				$PM_{2.5}$ (μg m^{-3})			
Fit	r	H	M	L	r	H	M	L	r	H	M	L	r	H	M	L
Ellipse	0.274	40.1	33.7	31.2	0.176	64.9	63.5	59.1	0.011	20.3	20.1	19.9	0.001	13.5	13.5	13.4
Gaussian kernel	0.361	48.2	41.7	33.4	0.257	63.7	57.0	51.3	0.017	20.3	20.2	19.9	0.038	13.6	13.2	12.9
Epanechnikov kernel	0.369	48.5	42.3	33.4	0.264	63.7	56.4	51.0	0.018	20.3	20.3	19.9	0.040	13.6	13.1	12.8
Gaussian kernel & elliptical shape	0.886	43.8	40.2	36.0	0.859	61.2	57.9	55.0	0.678	20.1	19.9		0.350	13.3	13.2	13.1
Gaussian fit by direction	0.961	46.9	40.0	33.3	0.946	63.3	57.8	52.4	0.976	20.2	20.0	19.8	0.862	13.9	13.5	13.2

* H = high, M = medium, L = Low.

m^{-3} for NO_2, O_3, PM_{10}, and $PM_{2.5}$, respectively, calculated with the kernels.

3.2. Second smoothing

3.2.1. Elliptical fit

The best advantage of the elliptical fit is that this is the simplest way to obtain the spatial distribution of concentrations at first sight. However, the kernel fit provides a more realistic distribution. Both fits were combined in the following analysis where the results of applying the Gaussian kernel were fitted with the elliptical function. Moreover, a variable background concentration was used to

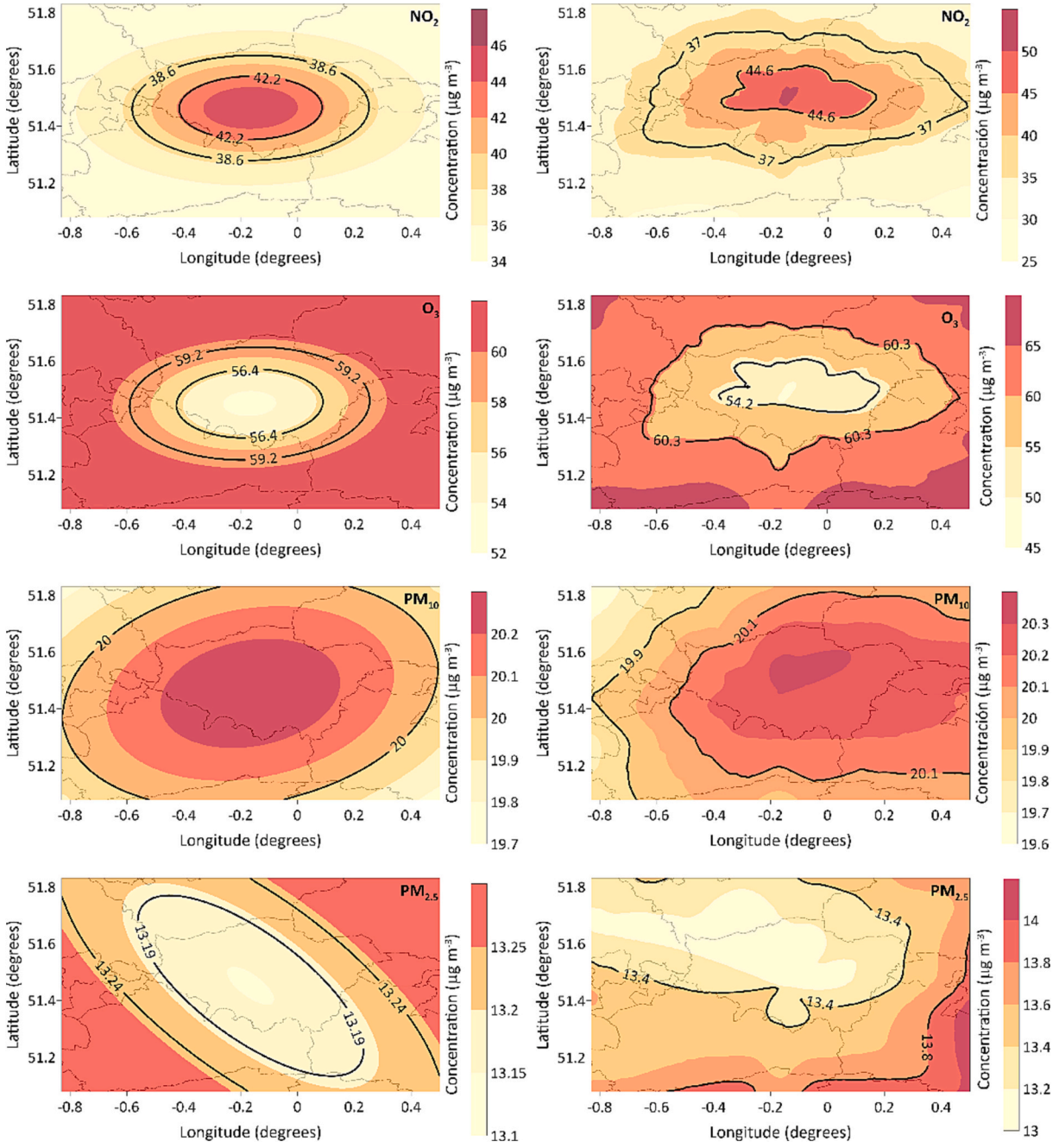

Fig. 4. a) Left column. Fit of concentrations calculated with the Gaussian kernel to an elliptical shape with a selection of background concentration. The black contours correspond to one and two thirds of the concentration interval with the background calculated. b) Right column. Gaussian fit of concentrations in a strip with variable direction. The black contours correspond to one and two thirds of the concentration range.

improve the fit. The chosen background was the one with the highest correlation coefficient. The values obtained for the background were 35, 62, 19.4, and 13.3 μg m^{-3} for NO_2, O_3, PM_{10}, and $PM_{2.5}$, respectively. Fig. 4 and Table 1 present the results. The contrast between the city centre and its surroundings is well defined for NO_2 and O_3. Moreover, the extension of both regions of high

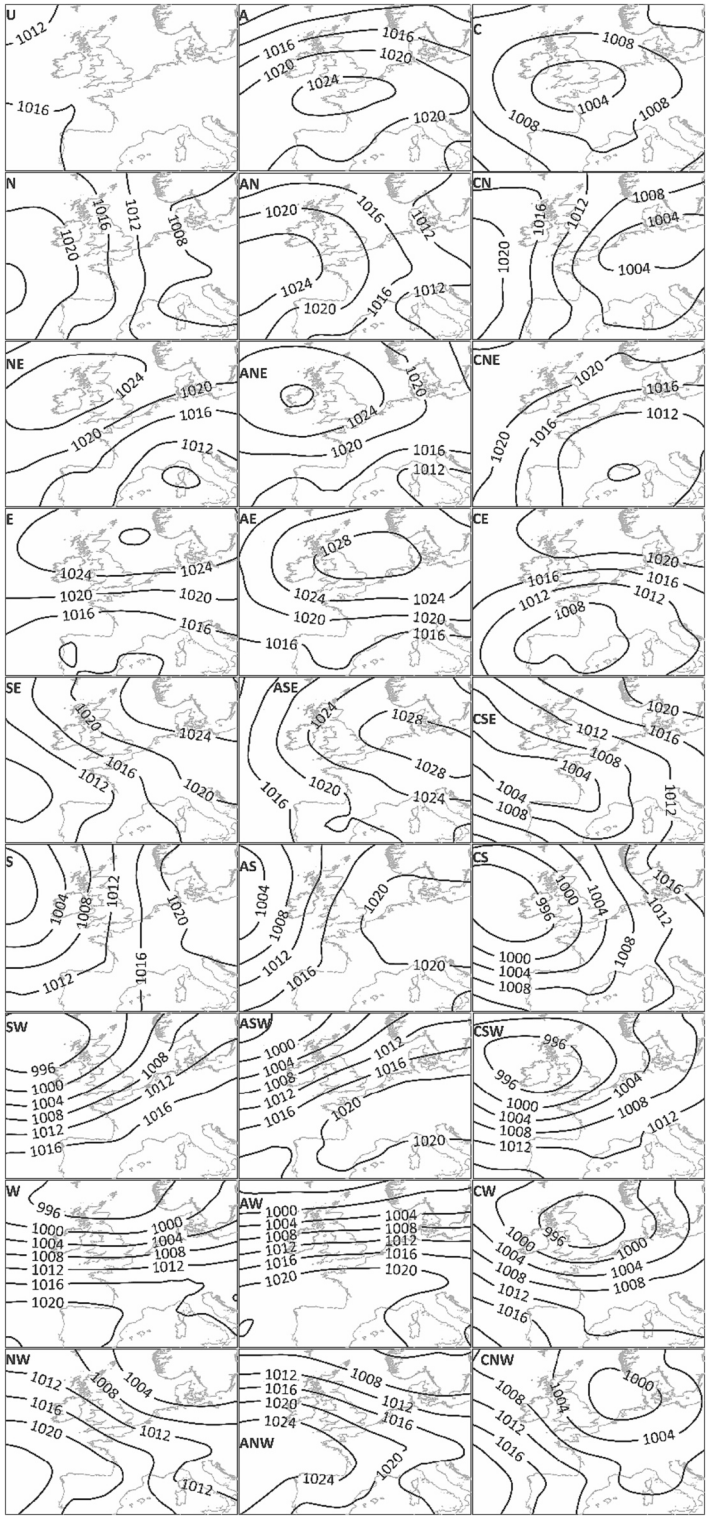

Fig. 5. Weather types for the period 2007–2011 –pressure in hPa.

concentrations is similar, revealing the anti-correlation of both pollutants. However, background concentrations were obtained outside the region studied for PM_{10} since the area of high concentrations is more extended than the area for NO_2 or O_3. Finally, the low value of the correlation coefficient for $PM_{2.5}$ indicates that the elliptical representation of this pollutant in Fig. 4 is only qualitative.

3.2.2. Directional fitting

This fit is presented in Fig. 4 in the right column. The first result is the breaking of the symmetry represented by the elliptical shape. Moreover, an expansion of the urban pollution island is observed for NO_2 and O_3 –in particular for the area with intermediate concentrations. For particulate matter, the distribution is simplified, with an expansion of the PM_{10} high concentrations to the east, whereas the expansion of the $PM_{2.5}$ low concentrations is observed to the northwest. In this analysis, the background concentration follows the direction investigated. However, in order to make the figures comparable to those of the former analyses, the concentration range was calculated and divided into three equal parts. These are the contours presented by black lines in the right column of Fig. 4. The agreement of the fit is improved following the correlation coefficients presented in Table 1.

3.3. Weather types

Fig. 5 presents the synoptic types calculated with the sea surface pressure in the period studied −2007-2011. One noticeable feature is the lack of isobars in the unclassified type, which indicates situations with low wind speeds. Another feature is the high number of isobars with pure and hybrid west types, revealing the high wind speeds linked with these situations. Moreover, the pressure centres in the hybrid types are close to the region centre in order to determine the corresponding wind direction.

The frequency of these types is presented in Fig. 6. Most of the situations are described by the anticyclonic type, followed by the westerly and south-westerly types, and the cyclonic type. The rest of the cyclonic types present very low frequencies, followed by the anticyclonic types, which were slightly higher, and directional types.

The annual distribution of these types is quite varied. For the most frequent types, the anticyclonic type is equally distributed throughout the year, albeit with some higher values in spring and autumn. The westerly type frequency presents two minima in spring and autumn, whereas the main maximum is reached in winter. For the south-westerly type, the frequency minimum is observed in spring, and low values were obtained in July, September, and October for the cyclonic type.

The pressure centres for hybrid types –together with those for the anticyclonic and cyclonic types– are presented in Fig. 7. For anticyclonic hybrid types, they are located in two groups, one to the east, mainly over the continent (AE, ASE, AS, ASW), whereas the second group is mainly over the sea (AW, ANW, AN, ANE). The centres of the cyclonic hybrid types are distributed regularly around the origin of the network used, which is presented in Fig. 2. However, a further two groups can be observed. The first, formed by CS, CSW, CW, CNW, and CN, is located in a narrow interval of latitudes at high latitudes, between 52 and 56°N, whereas types with an east flow,

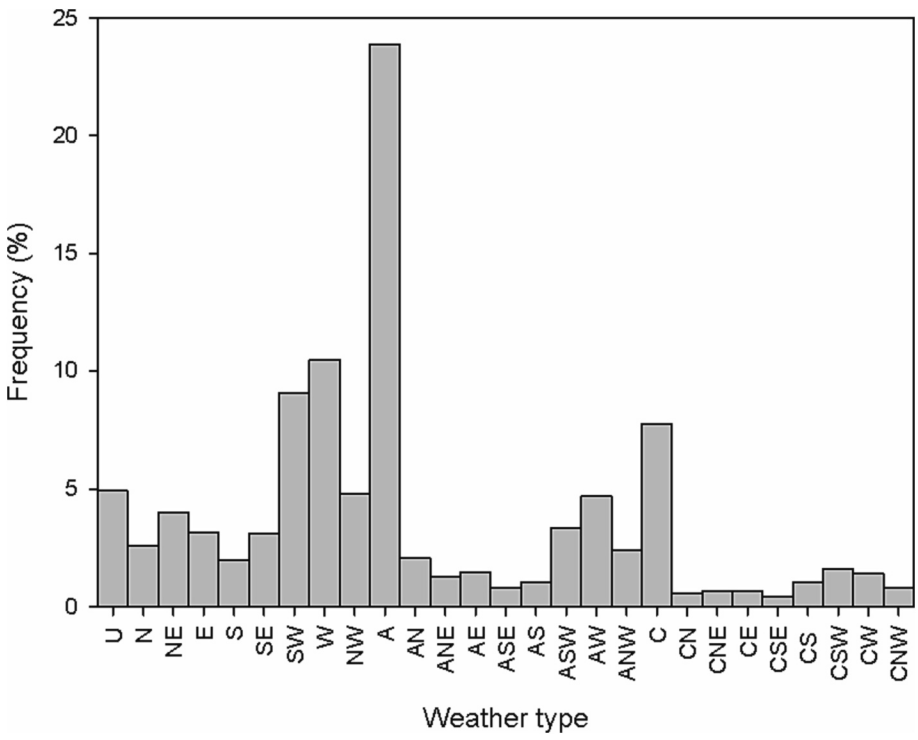

Fig. 6. Frequency of Lamb weather types in the period 2007–2011.

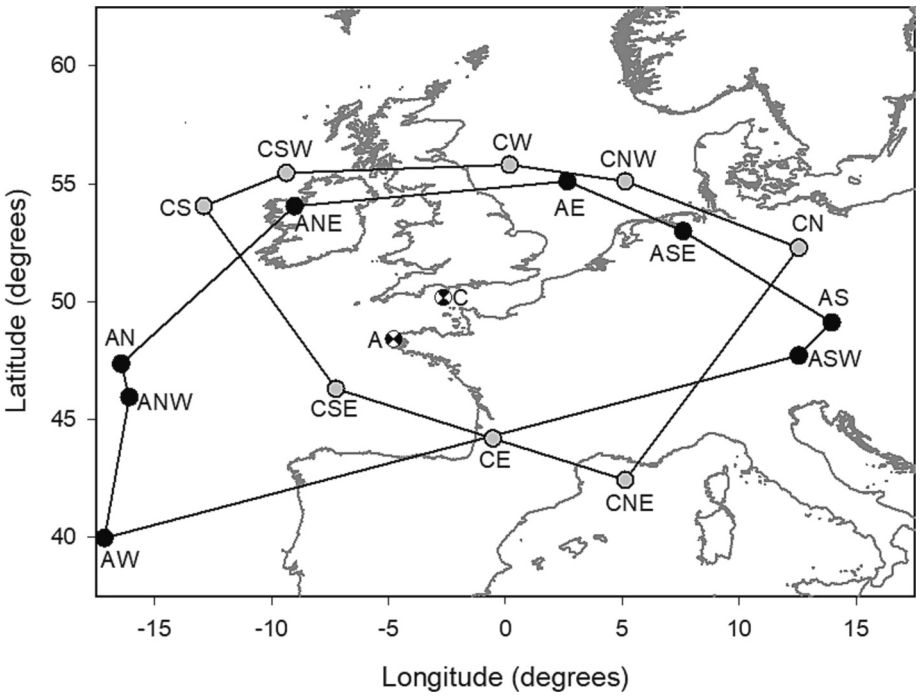

Fig. 7. Pressure centres for hybrid types together with anticyclonic and cyclonic types.

CNE, CE, and CSE, are grouped at low latitudes, between 42 and 47°N and in a narrower interval of longitudes. Finally, the pure anticyclonic and cyclonic types are located in the centre of the figure.

The concentration associated with these types is presented in Fig. 8. The average calculated with values from this figure is the highest for anticyclonic types for NO_2 (in the middle of the figure) and under directional types for O_3 (on the left of the figure). The average concentration is the lowest with directional types for PM_{10}, and with anticyclonic types for $PM_{2.5}$, although the contrast among the concentrations for the three groups of weather patterns is low. However, exceptional peaks can be seen. For instance, for directional patterns, high values are observed for NO_2 under SE and S types, and for PM_{10} and $PM_{2.5}$ for the SE type, and low O_3 values with the S type, with the NO_2 values being high in this case. For anticyclonic types, high concentrations are observed under the ASE type for NO_2 and PM_{10}, whereas O_3 concentrations are low with this type. Finally, for cyclonic types (on the right of the figure), high concentrations are observed for PM_{10} with CE and CSE types, and for $PM_{2.5}$ with the CSE type, whereas O_3 concentration was high for CE, and low for CS. One noticeable result of this analysis is the link between the low O_3 values and the high NO_2 and PM_{10} concentrations under the ASE pattern.

Although concentrations linked with the ASE type stand out, this is no frequent type. Since the most usual pattern is the anticyclonic type, Fig. 9 presents the concentration distribution for the days when the average concentration fell in the upper and lower quartiles. Rather than using the elliptical shape, the Gaussian kernel was used to smooth the concentration contours, since the urban pollution island was more poorly defined when using the elliptical shape. The shape is similar for NO_2 and O_3, revealing the city centre as the source of precursors whereas the high O_3 concentrations are located in the surrounding areas. Since the black lines are spaced as one third of the concentration range, there is a rapid change of concentration between the centre and its surroundings, except to the east, where average concentrations are fairly extended. Despite the narrow variation interval, PM_{10} concentrations present a contrasting pattern, since the upper quartile concentrations display a shape linked to the city. For this pollutant –and although the concentrations are quite similar in the region analysed– the highest values are in a small region, whereas the average values are more extended. However, this shape is lost for the lower quartile concentrations whose high values are to the east whereas the low values are to the west –with no influence of the city being revealed. Something similar is observed for $PM_{2.5}$. For this pollutant, certain low values are observed in the city for the upper quartile, whereas the lower quartile concentrations do not seem to be linked to the city centre.

Moreover, observations are found in autumn and winter for the upper quartile of NO_2 and particulate matter as well as for the lower quartile of O_3. The O_3 upper quartile is mainly found in spring. However, observations are found in spring and summer for the lower quartile of NO_2 and particulate matter. Similar representations are presented as supplementary material for the west weather type (Fig. S1), southwest weather type (Fig. S2), and cyclonic weather type (Fig. S3). These four types account for about 51% of weather situations. In general, the urban pollution island is well defined for NO_2 and O_3. However, this island appears in certain situations for particulate matter.

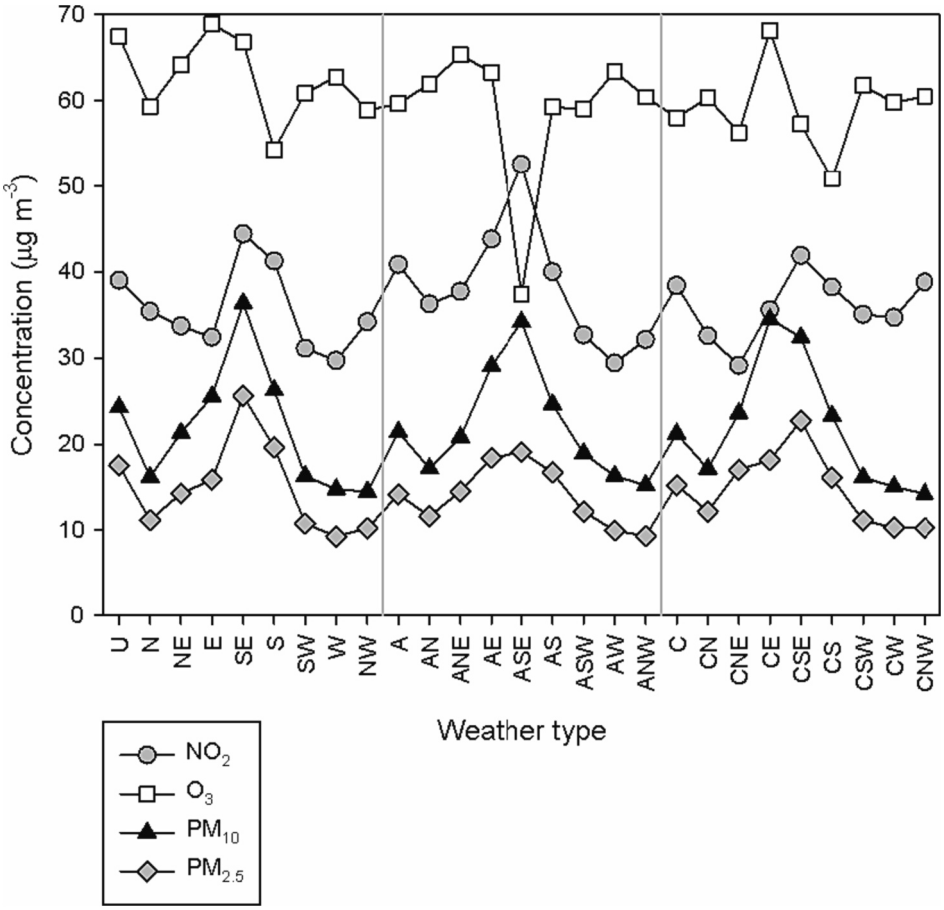

Fig. 8. Average concentrations in the region studied in the period 2007–2011 under Lamb weather types.

4. Discussion

4.1. The urban pollution island

This research applies the elliptical fit presented by Yao, Sun, Wang, Song, and Xu (2022a); Yao, Xu, Sun, and Wang (2022b). Said authors considered a threshold to separate rural and urban environments. The left column of Fig. 3 offers an initial step that did not consider background concentration, such that –as a result– ellipses are extended. However, background concentration may be considered, for instance, by the Gaussian smoothing presented in the middle column of Fig. 3, where the city and rural environments may be separated. In this case, the elliptical fit presented in the left column of Fig. 4 reveals that the ellipses are quite focused on the city for NO_2 and O_3, although the extension is higher for particulate matter, due to the low contrast between the city centre and its surroundings.

The Gaussian and Epanechnikov kernels were used by Donnelly, Misstear, and Broderick (2011) to smooth NO_2 concentrations with wind speed and direction at different sites in Ireland. The procedure is extended in this research to a spatial analysis where pollution contours are defined for NO_2 and O_3, whereas there is only a slight contrast between the city centre and its surroundings for particulate matter. Concentration contours are smoother for the Gaussian kernel. Moreover, pollutants may be grouped, since NO_2 and PM_{10} present high values in the city centre, whereas this is a site of low concentrations for O_3 and $PM_{2.5}$.

Hereher, Eissa, Alqasemi, and El Kenawy (2022) studied pollution in Greater Cairo and considered a classification formed by three pollution degrees. This is a simple and illustrative procedure to highlight urban air pollution. In the current paper, two boundaries were suggested to establish three pollution regions, with low, moderate and high concentrations, the means of which are presented in Table 1.

Zhu et al. (2020) used the modified sigmoid function to establish concentric rings designed to calculate changes in $PM_{2.5}$ concentrations from the city centre to rural areas. This is a simple model to establish the urban pollution island, although with the inconvenience that it should be applied to a near-circular city. Schmitt et al. (2023) considered elliptical shapes to establish the urban pattern. This approach improves the model since the city shape is simplified and the ellipse orientation follows the concentration distribution. A Gaussian fit following the direction is an original contribution of this research, whose main consequence is determining

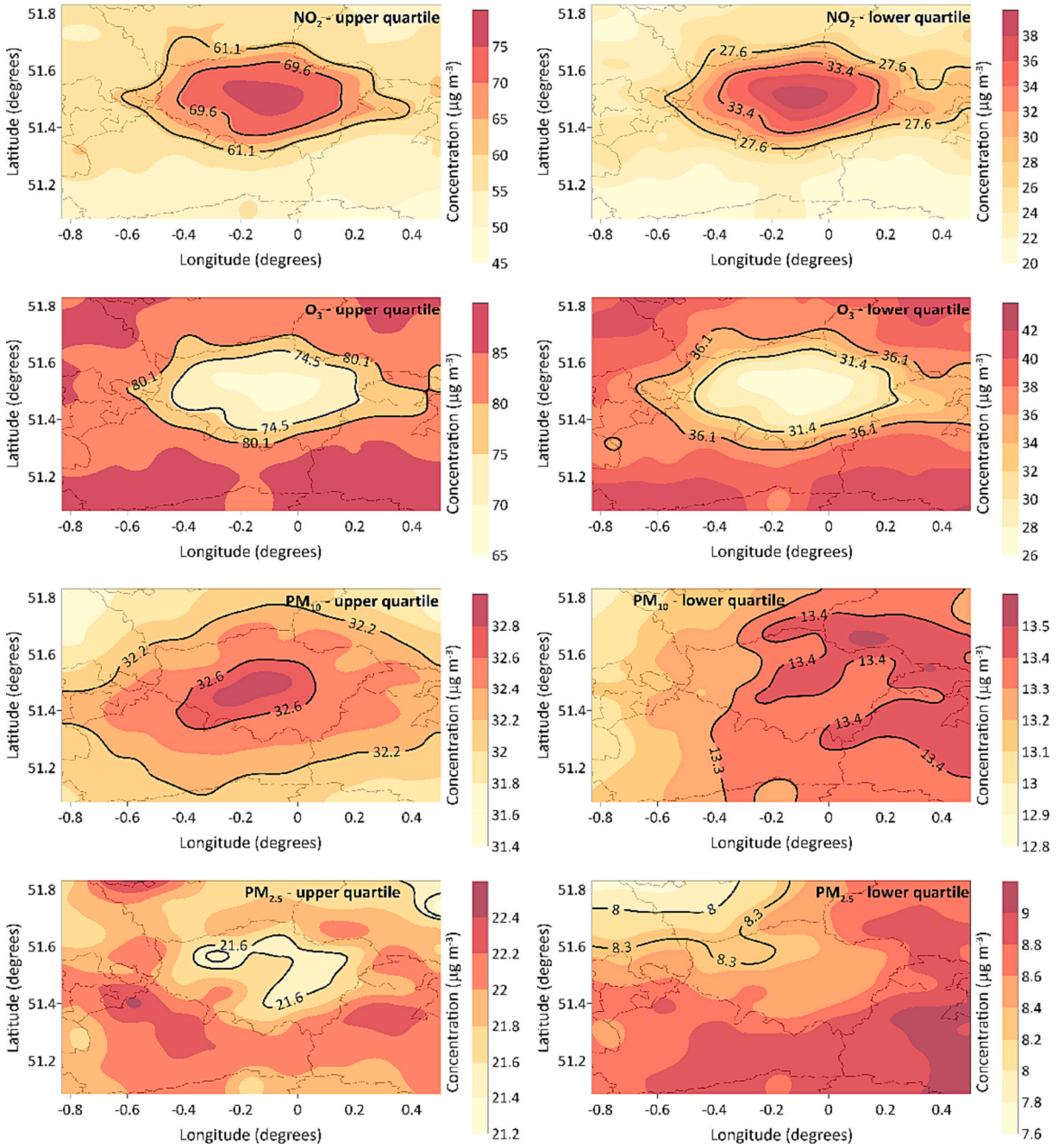

Fig. 9. Concentration distribution corresponding to an anticyclonic pattern for daily averages in the upper quartile on the left and below the lower quartile on the right. The black lines represent the boundaries of one third the difference between the maximum (for NO_2 and PM_{10}) or the minimum (for O_3 and $PM_{2.5}$) and the background concentration represented by the average of the corners.

background concentrations following the direction and expansion of the concentration boundaries. The non-uniformity of background concentrations has already been presented, since Li, Zhou, Lenschow, Cheng, and Dou (2020) introduced the contrast between two rural environments for the Beijing urban island. They divided rural stations between northern and southern rural stations and obtained a daily pattern with noticeable differences for $PM_{2.5}$ concentrations at night, when southern concentrations were around 110 μg m^{-3}, whereas northern concentrations may be even slightly below 60 μg m^{-3}. In this research, background concentrations are radially distributed from the city centre, which was calculated by weighting the concentrations with the coordinates of the grid used.

4.2. Weather types

Abbassi, Ahmadikia, and Baniasadi (2022) investigated the impact of wind speed –which is a local variable– on the urban heat and pollution island. This paper considers synoptic patterns –which is a regional variable– as a meteorological factor, whose influence on the urban pollution island should be explored.

De Luca et al. (2019) modelled the evolution of certain types over the British Isles in the period 2010–2100. At the beginning of the series, values were around 25% for the A type in summer, slightly lower for the W type in winter, around 20% for the C type in autumn, and around 15% for the S type in spring. Although seasons are not separated in the current analysis, the frequency is similar for the A type, whereas lower frequencies are observed for the remaining types. Fernández-Granja, Casanueva, Bedia, and Fernandez (2021) considered the same region for the period 1981–2010, and found the A type to be the most frequent (20.35%), followed by C types (13.44%), W (11.44%) and SW (10.46%). In this study, frequency is lower for the cyclonic type, although the calculation period is much smaller.

The network shift implies new meteorological conditions and the frequencies of the types will be different even if the displacement is small. Fealy and Mills (2018) considered two networks over the British Isles with a slight shift to investigate the period 1948–2016 and calculated changes in synoptic type frequencies.

Pérez and García (2023) used the same pressure network to study synoptic patterns over the Iberian Peninsula in the period 1948–2021. Although the pressure maps are similar, some differences can be seen. For instance, the pressure centres are more extended over the Iberian Peninsula for the anticyclonic and cyclonic types. The number of isobars is high in the westerly types presented in Fig. 5, indicating high wind speeds. This is similar for the Iberian Peninsula for directional and anticyclonic types. However, the isobar number is lower for westerly cyclonic types.

Although the anticyclonic type is the most frequent in the two regions, the frequency is higher over the British Isles, followed by southwest and west types. Over the Iberian Peninsula, the second most frequent type is the unclassified type, followed by the cyclonic type –which is the last of the most frequent types over Britain. Moreover, three anticyclonic pressure centres of hybrid types are located to the east of the region for the Iberian Peninsula, whereas only two were obtained for Britain. As regards the cyclonic centres of hybrid types, most are around the Iberian Peninsula and two were near the limits of the region to the south. Over Britain, these cyclonic centres are confined in two groups, one for high latitudes, and the other for low latitudes.

Giaccone, Fratianni, Cortesi, and González-Hidalgo (2019) considered weather types in NW Italy in the period 2003–2014. However, they considered ten weather types by grouping hybrid types as pure directional types –following Trigo and DaCamara (2000). The most frequent was the anticyclonic type (19%) followed by the north-easterly type (16%), and the northerly type (12%).

4.3. The urban pollution island and weather types

Liao, Wu, Zhou, Wang, and Chen (2021) described ozone concentrations in Guangzhou, southern China, in the period 2006–2016. The result is that several types, such as A or AS, were linked with high O_3 concentrations, whereas types such as C or CE were related with low O_3 concentrations. Giaccone, Fratianni, Cortesi, and González-Hidalgo (2019) related the highest daily ozone concentrations in NW Italy with easterly and south-easterly patterns, whereas the lowest daily ozone concentrations were obtained with cyclonic and westerly types.

Guo et al. (2022) investigated $PM_{2.5}$ pollution in the Sichuan basin in China. They considered several meteorological variables such as the boundary layer height, surface wind speed, or temperature inversions. Moreover, they used a similar network to establish synoptic types and found that heavy pollution events were linked with low pressure over the north west of the site and with southerly transport.

Pollution transport contribution has been highlighted in several studies. Francis et al. (2011) pointed to three possible mechanisms as being responsible for O_3 concentrations observed over South East England during the August 2003 heatwave. The first is transport from Europe under a high pressure system. The second is the convergence of westerly and easterly surface winds, and the third is the entrainment of ozone-rich air from the free troposphere. Graham et al. (2020) indicated that easterly, south-easterly and southerly wind directions were linked with high background concentrations of particulate matter in the United Kingdom, which could be transported from continental Europe. The current research reveals the high NO_2 concentrations and low O_3 values associated with the ASE flow. High O_3 concentrations were obtained with E, SE, and CE flows. These values could be associated with air flow from the continent to the British Isles.

5. Conclusions

The elliptical shape offers an initial approach to the urban pollution island, although its applications must be preceded by determining background concentrations. Concentration smoothing is necessary to observe the pattern of concentrations. The Gaussian kernel provided a smoother shape when compared to the Epanechnikov kernel.

The urban pollution island was well defined for NO_2 and O_3 with the opposite pattern, i.e. the city is an NO_2 source but an O_3 sink. An urban pollution island is not observed for particulate matter since the contrast between the city and its surroundings is very low. Moreover, two pollutant pairs may be formed by the spatial distribution of concentrations; the first is formed by NO_2 and PM_{10} and the second by O_3 and $PM_{2.5}$.

Background concentrations were established by a second smoothing performed with the concentrations calculated by the Gaussian kernel. Two procedures were used. The first is based on an elliptical fit that simplifies the pollution island shape, whose impact is

around 7 μg m^{-3} for NO_2 and O_3 with a longitudinal extension. However, the distribution of particulate matter does not seem to be controlled by the city. The second procedure is a directional smoothing where the region of intermediate concentrations increased compared to that obtained with the elliptical one.

The distribution of weather types was quite irregular. The most frequent synoptic pattern was anticyclonic –around 24%. This frequency was similar to that for all the directional westerly types. Frequency of the cyclonic type was around 7%, which was similar to that of all the hybrid cyclonic types.

This detailed flow distribution revealed that average NO_2 values are below average O_3 values, except for the ASE flow, which presents lower O_3 values than those for NO_2. SE and CSE also presented high NO_2 values, which may be justified by NO_2 transport from the continent in these three types. High concentrations of particulate matter are linked with some east flows and could also be related with transport from the continent. Low concentrations of particulate matter were linked to westerly types, i.e. flows from the sea. These synoptic maps revealed a high isobar concentration and, consequently, high winds.

The shape of the urban pollution island was studied under the most frequent weather types. Shapes are similar to those when types are not separated, since the difference is in the concentrations. Moreover, the urban pollution island is observed for both high and low concentrations for NO_2 and O_3, whereas this island is reached for PM_{10} in specific occasions.

This paper selects pollutants following the spatial distribution of their concentrations, and three areas are considered according to the pollution values. Key information is therefore provided to air pollution managers to enable them to improve control measures on specific pollutants and at specific sites. The annual evolution of the urban pollution island lays outside the scope of this paper and should be the objective of further research, as should a detailed study of the annual evolution of weather types. Additional meteorological variables –and even satellite information– could be added in order to gain clearer insights into the urban pollution island and so enable better decisions to be taken for safeguarding human health.

Funding

This research received no external funding.

Credit authorship contribution statement

Isidro A. Pérez: Conceptualization, Methodology, Research, Writing – original draft. Mª. Ángeles García: Writing – review & editing. Saeed Rasekhi: Writing – review & editing. Fatemeh Pazoki: Writing – review & editing.

Declaration of competing interest

The authors declare that they have no known competing financial interests or personal relationships that might influence the work reported in this paper.

Data availability

The air pollution data may be downloaded from the Medical & Environmental Data Mash-up Infrastructure project at https://www.data-mashup.org.uk/research-projects/statistical-downscaling-ofgridded-air-quality-data/. The NCEP-NCAR Reanalysis 1 data of sea level pressure can be downloaded from the NOAA website at https://psl.noaa.gov.

Appendix A. Supplementary data

Supplementary data to this article can be found online at https://doi.org/10.1016/j.uclim.2024.101834.

References

Abbassi, Y., Ahmadikia, H., Baniasadi, E., 2022. Impact of wind speed on urban heat and pollution islands. Urban Clim. 44, 101200 https://doi.org/10.1016/j.uclim.2022.101200.

Ashraf, H., El Seoud, T.A., Sodoudi, S., El Zafarany, A., 2023. Anisotropic surface urban heat island in Cairo, Egypt: a spatiotemporal analysis of local climate change from 2000 to 2021. Civ. Eng. Archit. 11, 331–350. https://doi.org/10.13189/cea.2023.110127.

Bakaeva, N., Le, M.T., 2022. Determination of urban pollution islands by using remote sensing technology in Moscow, Russia. Ecol. Inform. 67, 101493 https://doi.org/10.1016/j.ecoinf.2021.101493.

Birim, N.G., Turhan, C., Atalay, A.S., Gokcen, Akkurt G., 2023. The influence of meteorological parameters on PM_{10}: a statistical analysis of an urban and rural environment in Izmir/Türkiye. Atmosphere 14. https://doi.org/10.3390/atmos14030421 art. no. 421.

Cao, W., Rohli, R.V., Han, F., Vega, A.J., Bushra, N., Nyman, J.A., 2021. Atmospheric circulation regimes for prescribed burns along the U.S. Gulf of Mexico coast. Appl. Geogr. 136, 102587 https://doi.org/10.1016/j.apgeog.2021.102587.

Chen, X., Wang, N., Wang, G., Wang, Z., Chen, H., Cheng, C., Li, M., Zheng, L., Wu, L., Zhang, Q., Tang, M., Huang, B., Wang, X., Zhou, Z., 2022. The influence of synoptic weather patterns on spatiotemporal characteristics of ozone Pollution across Pearl River Delta of southern China. J. Geophys. Res.-Atmos. 127 https://doi.org/10.1029/2022JD037121 e2022JD037121.

De Luca, P., Harpham, C., Wilby, R.L., Hillier, J.K., Franzke, C.L.E., Leckebusch, G.C., 2019. Past and projected weather pattern persistence with associated multi-hazards in the British Isles. Atmosphere 10, 577. https://doi.org/10.3390/atmos10100577.

Donnelly, A., Misstear, B., Broderick, B., 2011. Application of nonparametric regression methods to study the relationship between NO2 concentrations and local wind direction and speed at background sites. Sci. Total Environ. 409, 1134–1144. https://doi.org/10.1016/j.scitotenv.2010.12.001.
Droste, A.M., Steeneveld, G.J., Holtslag, A.A.M., 2018. Introducing the urban wind island effect. Environ. Res. Lett. 13, 094007 https://doi.org/10.1088/1748-9326/aad8ef.
Fealy, R., Mills, G., 2018. Deriving Lamb weather types suited to regional climate studies: a case study on the synoptic origins of precipitation over Ireland. Int. J. Climatol. 38, 3439–3448. https://doi.org/10.1002/joc.5495.
Fernández-Duque, B., Pérez, I.A., García, M.Á., Pardo, N., Sánchez, M.L., 2019. Annual and seasonal cycles of CO_2 and CH_4 in a Mediterranean Spanish environment using different kernel functions. Stoch. Environ. Res. Risk Assess. 33 (3), 915–930. https://doi.org/10.1007/s00477-019-01655-5.
Fernández-Granja, J.A., Casanueva, A., Bedia, J., Fernandez, J., 2021. Improved atmospheric circulation over Europe by the new generation of CMIP6 earth system models. Climate Dynam. 56, 3527–3540. https://doi.org/10.1007/s00382-021-05652-9.
Fernández-Granja, J.A., Brands, S., Bedia, J., Casanueva, A., Fernández, J., 2023. Exploring the limits of the Jenkinson–Collison weather types classification scheme: a global assessment based on various reanalyses. Climate Dynam. 61, 1829–1845. https://doi.org/10.1007/s00382-022-06658-7.
Francis, X.V., Chemel, C., Sokhi, R.S., Norton, E.G., Ricketts, H.M.A., Fisher, B.E.A., 2011. Mechanisms responsible for the build-up of ozone over South East England during the august 2003 heatwave. Atmos. Environ. 45, 6880–6890. https://doi.org/10.1016/j.atmosenv.2011.04.035.
Giaccone, E., Fratianni, S., Cortesi, N., González-Hidalgo, J.C., 2019. Surface ozone concentration and its relation with weather types in NW Italy, 2003-2014. Climate Res. 77, 77–89. https://doi.org/10.3354/cr01546.
Graham, A.M., Pringle, K.J., Arnold, S.R., Pope, R.J., Vieno, M., Butt, E.W., Conibear, L., Stirling, E.L., McQuaid, J.B., 2020. Impact of weather types on UK ambient particulate matter concentrations. Atmos. Environ. X 5, 100061 https://doi.org/10.1016/j.aeaoa.2019.100061.
Guo, Q., Wu, D., Yu, C., Wang, T., Ji, M., Wang, X., 2022. Impacts of meteorological parameters on the occurrence of air pollution episodes in the Sichuan basin. J. Environ. Sci. 114, 308–321. https://doi.org/10.1016/j.jes.2021.09.006.
Han, H., Zhang, L., Liu, Z., Yue, X., Shu, L., Wang, X., Zhang, Y., 2023. Narrowing differences in urban and nonurban surface ozone in the northern hemisphere over 1990-2020. Environ. Sci. Technol. Lett. 10, 410–417. https://doi.org/10.1021/acs.estlett.3c00105.
Hereher, M., Eissa, R., Alqasemi, A., El Kenawy, A.M., 2022. Assessment of air pollution at greater Cairo in relation to the spatial variability of surface urban heat island. Environ. Sci. Pollut. Res. 29, 21412–21425. https://doi.org/10.1007/s11356-021-17383-9.
Ivanovski, M., Alatič, K., Urbancl, D., Simonič, M., Goričanec, D., Vončina, R., 2023. Assessment of air pollution in different areas (urban, suburban, and rural) in Slovenia from 2017 to 2021. Atmosphere 14, 578. https://doi.org/10.3390/atmos14030578.
Jenkinson, A.F., Collison, F.P., 1977. An initial climatology of gales over the North Sea. Synoptic climatology branch memorandum no. 62. Meteorological office, Bracknelly, UK.
Karlický, J., Huszár, P., Nováková, T., Belda, M., Švábik, F., Doubalová, J., Halenka, T., 2020. The "urban meteorology island": a multi-model ensemble analysis. Atmos. Chem. Phys. 20, 15061–15077. https://doi.org/10.5194/acp-20-15061-2020.
Lamb, H.H., 1972. British Isles weather types and a register of daily sequence of circulation patterns, 1861–1971. Geophysical Memoir 116. HMSO, London.
Li, J., Zhou, M., Lenschow, D.H., Cheng, Z., Dou, Y., 2020. Observed relationships between the urban heat island, urban pollution island, and downward longwave radiation in the Beijing area. Earth Space Sci. 7 https://doi.org/10.1029/2020EA001100 e2020EA001100.
Liang, L., Daniels, J., Bailey, C., Hu, L., Phillips, R., South, J., 2023. Integrating low-cost sensor monitoring, satellite mapping, and geospatial artificial intelligence for intra-urban air pollution predictions. Environ. Pollut. 331, 121832 https://doi.org/10.1016/j.envpol.2023.121832.
Liao, W., Wu, L., Zhou, S., Wang, X., Chen, D., 2021. Impact of synoptic weather types on ground-level ozone concentrations in Guangzhou, China. Asia-Pac. J. Atmos. Sci. 57, 169–180. https://doi.org/10.1007/s13143-020-00186-2.
Medical & Environmental Data Mash-up Infrastructure, 2023. https://www.data-mashup.org.uk/research-projects/statistical-downscaling-ofgridded-air-quality-data/. Last access 20 June 2023.
Milelli, M., Bassani, F., Garbero, V., Poggi, D., von Hardenberg, J., Ridolfi, L., 2023. Characterization of the urban heat and dry island effects in the Turin metropolitan area. Urban Clim. 47, 101397 https://doi.org/10.1016/j.uclim.2022.101397.
Mohammad, P., Goswami, A., 2023. Exploring different indicators for quantifying surface urban heat and cool island together: a case study over two metropolitan cities of India. Environ. Dev. Sustain. 25, 10857–10878. https://doi.org/10.1007/s10668-022-02509-x.
Mukhopadhyay, S., Sahu, S.K., 2018. A Bayesian spatiotemporal model to estimate long-term exposure to outdoor air pollution at coarser administrative geographies in England and Wales. J. R. Stat. Soc. Ser. A-Stat. Soc. 181, 465–486. https://doi.org/10.1111/rssa.12299.
Osipova, O.P., Osipov, E.Y., 2022. Objective classification of weather types for the eastern Siberia over the 1970–2020 period using the Jenkinson and Collison method. Atmos. Res. 277, 106291 https://doi.org/10.1016/j.atmosres.2022.106291.
Otero, N., Sillmann, J., Butler, T., 2018. Assessment of an extended version of the Jenkinson–Collison classification on CMIP5 models over Europe. Climate Dynam. 50, 1559–1579. https://doi.org/10.1007/s00382-017-3705-y.
Pérez, I.A., García, M.Á., 2023. Climate change in the Iberian Peninsula by weather types and temperature. Atmos. Res. 284, 106596 https://doi.org/10.1016/j.atmosres.2022.106596.
Putniković, S., Tošić, I., 2018. Relationship between atmospheric circulation weather types and seasonal precipitation in Serbia. Meteorol. Atmos. Phys. 130, 393–403. https://doi.org/10.1007/s00703-017-0524-y.
Qin, X., Dong, X., Tao, Z., Wei, R., Zhang, H., Guo, Q., 2023. Tracing the transboundary transport of atmospheric particulate bound mercury driven by the east Asian monsoon. J. Hazard. Mater. 446, 130678 https://doi.org/10.1016/j.jhazmat.2022.130678.
Salinger, M.J., Verdi, L., Dalla, Marta A., Dalu, G., Baldi, M., Messeri, G., Vallorani, R., Morabito, M., Crisci, A., Altobelli, F., Orlandini, S., Gozzini, B., Messeri, A., 2022. Linking maize yields in Veneto Italy, to large-scale atmospheric variability, circulation regimes and weather types. J. Agric. Sci. 160, 423–439. https://doi.org/10.1017/S0021859622000545.
Sarricolea, P., Meseguer-Ruiz, O., Martín-Vide, J., Outeiro, L., 2018. Trends in the frequency of synoptic types in Central-Southern Chile in the period 1961–2012 using the Jenkinson and Collison synoptic classification. Theor. Appl. Climatol. 134, 193–204. https://doi.org/10.1007/s00704-017-2268-5.
Schmitt, A., Uth, P., Standfuß, I., Heider, B., Siedentop, S., Taubenböck, H., 2023. Quantitative assessment and comparison of urban patterns in Germany and the United States. Comput. Environ. Urban. Syst. 100, 101920 https://doi.org/10.1016/j.compenvurbsys.2022.101920.
Tammekivi, T., Kaasik, M., Hamer, P., Santos, G.S., Šteinberga, I., 2023. Air pollution situation in small towns, including winter resorts: a comparative study of three cases in northern Europe. Air Qual. Atmos. Health 16, 945–961. https://doi.org/10.1007/s11869-023-01315-2.
Trigo, R.M., DaCamara, C.C., 2000. Circulation weather types and their influence on the precipitation regime in Portugal. Int. J. Climatol. 20, 1559–1581. https://doi.org/10.1002/1097-0088(20001115)20:13<1559::AID-JOC555>3.0.CO;2-5.
Ulpiani, G., 2021. On the linkage between urban heat island and urban pollution island: three-decade literature review towards a conceptual framework. Sci. Total Environ. 751, 141727 https://doi.org/10.1016/j.scitotenv.2020.141727.
Yan, Y., Zhou, Y., Kong, S., Lin, J., Wu, J., Zheng, H., Zhang, Z., Song, A., Bai, Y., Ling, Z., Liu, D., Zhao, T., 2021. Effectiveness of emission control in reducing $PM_{2.5}$ pollution in Central China during winter haze episodes under various potential synoptic controls. Atmos. Chem. Phys. 21, 3143–3162. https://doi.org/10.5194/acp-21-3143-2021.
Yao, L., Sun, S., Wang, Y., Song, C., Xu, Y., 2022a. New insight into the urban $PM_{2.5}$ pollution island effect enabled by the Gaussian surface fitting model: a case study in a mega urban agglomeration region of China. Int. J. Appl. Earth Obs. Geoinf. 113, 102982 https://doi.org/10.1016/j.jag.2022.102982.
Yao, L., Xu, Y., Sun, S., Wang, Y., 2022b. Revisiting $PM_{2.5}$ pollution along urban-rural gradient and its coupling with urbanization process, a new perspective from urban pollution island analysis. Urban Clim. 45, 101270 https://doi.org/10.1016/j.uclim.2022.101270.
Yin, S., Hua, J., Ren, C., Liu, S., Lin, H., Huang, S., Wang, K., Ma, J., Xiao, Y., 2023. Impact of synoptic condition on urban microclimate variation: a measurement study in a humid subtropical city during summer season. Urban Clim. 47, 101350 https://doi.org/10.1016/j.uclim.2022.101350.
Zhu, L., Huang, Q., Ren, Q., Yue, H., Jiao, C., He, C., 2020. Identifying urban haze islands and extracting their spatial features. Ecol. Indic. 115, 106385 https://doi.org/10.1016/j.ecolind.2020.106385.